REVISION 1: Ab initio investigations of dioctahedral interlayer-deficient mica: Modeling particles of illite found within gas shale

Dawn Geatches[1]*, Douglas McCarty[2]
and Jennifer Wilcox[1]

[1] Energy Resources Engineering, 367 Panama Street, Stanford, CA 94305, USA;

[2] Chevron ETC, 3901 Briarpark, Houston, TX 77042, USA.

ABSTRACT

The focus of the study presented here is the illite component of the clay mineral components found within gas shale, specifically the creation of robust, atomistic models of illite particles bearing characteristics of the $2M_1$ polytype. The template for the illite models is derived from crystallographic data, which is used together with the general formula, $K_{1.67}(Al_{3.29}Fe_{0.38}Mg_{0.32})[(Si_{6.68}\ Al_{1.32})O_{20}(OH)_4]$ to create different particles of illite, each containing potassium plus either ammonium (NH_4^+)

---

*Email: geatches@stanford.edu

or hydronium (H_3O^+) ions, or water molecules in two different proportions. These atomistic models are optimized from first principles using plane waves and pseudo potentials within the formalism of density functional theory (DFT). The resulting lattice lengths, lattice dynamics in the form of infrared frequencies, positions of interlayer molecules and simulated X-ray powder diffraction (XRPD) patterns are analyzed with reference to the available experimental data. We conclude that all four illite models display properties that fall within the range of available experimental data, and that therefore these are state-of-the-art atomistic illites, ready for use in further studies. Furthermore, the analytical data from these models will enable the characterization of physical samples of illite with varying interlayer constituents.

Keywords DFT, shale, ammonium ions, hydronium ions, $2M_1$-illite, interlayer-deficient mica

INTRODUCTION

Investigating the atomistic structure of illite particles might appear to be far-removed from energy production and long-term CO_2 storage, but essentially, it is much closer to both these issues than is immediately apparent. The feasibility of using CO_2 for enhanced methane recovery from gas shale beds, and then using these exhausted shale beds as long-term storage for sequestered CO_2, (Wilcox 2012) depends on many factors at multiple length-scales, one of which is how the components of gas shale interact with CO_2 and CH_4. Such interactions could be chemical in nature, hence their investigation requires robust, atomistic models that would allow for the nature of the interactions to be identified. The atomistic structure of clay minerals determines the surfaces experienced by contact molecules, which in turn governs the interactions between them. Illite has a total surface area of approximately 85m^2/g, (Macht et al. 2011) and within gas shales, illite comprises up to 20% of the clay minerals, which themselves constitute up to 50% of the overall shale contents, (Środoń 2009) and hence theoretically there is enormous potential for interactions between the clay mineral surfaces and their environments. However, before the investigation of surface/molecule interactions comes the creation of the illite models themselves, and although there are in-depth DFT studies of the cation distribution in dioctahedral phyllosilicates (Escamilla-Roa et al. 2013), (Hernàndez-Laguna et al. 2006) for example, a category that includes the illite series, to-date we have not found any DFT studies specifically concerning particles created from $2M_1$ illite with various interlayer molecules.

Illite is classed as a '...dioctahedral interlayer-deficient mica..' (Fleet 2003) characterized by non-swelling behavior and an interlayer dominated by potassium ions. Each layer consists of tetrahedral-octahedral-tetrahedral (TOT) sheets composed of (mainly) $T_2^{4+}O_5$ and $R_2^{3+}O_5$, respectively where T^{4+} is usually Si^{4+} and R^{3+} is predominantly Al^{3+}. Substitutions of the T-cations by Al^{3+} and O-cations by Fe^{2+}/Fe^{3+} and Mg^{2+} produces a negatively charged TOT layer. The negative charge is then balanced by positive interlayer cations, which, in the case of illite are mainly K^+, (well documented) NH^{4+} (Lindgreen et al. 1991a; 1991b) and H_3O^+ (Nieto et al. 2010). A general formula for potassium-interlayer, $2M_1$ illite is $K_{1.67}(Al_{3.29}Fe_{0.38}Mg_{0.32})[(Si_{6.68}Al_{1.32})O_{20}(OH)_4]$ (Zöller and Brockamp 1997). The octahedral layer cations fill two of three possible octahedral sites, hence the description 'dioctahedral'. Within the mica group of minerals, there are six polytypes formed by the various stacking possibilities of the TOT layers with each other, that is, the TOT sheets are all translated or rotated to the same degree, but relative to another TOT layer could be variously translated or rotated (Nespolo 2001). Fortunately, there is experimental data concerning the polytypes of illite reporting that it occurs as two main polytypes, $1M$ and $2M_1$ (Drits and Zviagina 2009). Zöller and Brockamp, (1997) suggest that these polytypes are different minerals with different compositions but we will refer to them as 'polytypes' (of illite) in this study.

In the Barnett shale, illite is the end product of diagenesis (Liming et al. 2012) and forms on the transformation or 'illitization' of smectites (Lausen et al. 1999; Lindgreen 1991; Eslinger and Pevear 1988). A consideration of the formation of shale reveals the existence of close contacts between organic matter and clay particles (Lash and Blood 2004), at least during its formation, if not also at its maturation (Williams and Ferrell 1991; Williams et al. 1992). Organic matter has been proposed as the source of ammonium (Stevenson 1960; Drits et al. 1997) as fixed interlayer molecules in illites, where the NH_4^+ is evidence of hydrocarbon generation. Higashi (1982) described NH_4^+ dominant mica as 'tobelite', and Wilson et al.(1992) characterized tobelitic veins in black shale (Utah). A 1966 study by Hower and Mowatt (1966) and references within, state that most illite-bearing materials contain the $2M_1$ polytype. A more recent study by Pevear (1999) identifies the illite polytypes within shale as $1M$ (including the disordered $1M$ group known as $1M_d$) and $2M_1$, with the former being the type found within diagenetic shale and the latter in detrital mica. Nieto et al. (2010) in their investigation of the role of H_3O^+ in the crystal structure of illite, found that the main polytpes were $2M_1$ and $1M$. The purpose of their study was to determine the crystal structure of illite depending on whether the interlayer species were water molecules or hydronium ions, as, according to them, 'In spite of decades of research on the subject, the crystal structure of illite is still poorly understood'. The presence of H_3O^+ was originally proposed by Brown and Norrish (1952) who postulated that oxonium (i.e., hydronium) ions could substitute for K^+ ions within the interlayers of illite. Their analysis suggested that water molecules are present between the non-expandable illite layers, both substituting K^+ ions and forming '..lenses of water'.

For the investigation we present here, we have chosen the characteristics of illite pertinent to that found within shale beds, because (in subsequent studies) we intend to address the wider research questions involving enhanced methane recovery from gas shales, and long-term storage of captured CO_2 in exhausted shale beds. It seems highly probable that all of the interlayer environments previously mentioned could be found within illite, and that if theoretical analyses such as lattice parameters, infrared (IR) frequencies and X-ray powder diffraction (XRPD) patterns were available, they could help identify and distinguish between the various types in physical samples. To these ends the study presented here forms the second part of two, concurrent, first-principle investigations of polytypes of illite, and a third may follow focussing on the disordered, $1M_d$ polytype. The first concentrated on various forms of $1M$ illite that might be found within gas shale, namely, single layers of illite both trans and cis vacant and double layers or 'sandwiches' of illite representing I-I fragments in all-trans, all-cis and mixed trans/cis combinations. The relative optimal positions of the tetrahedral Al^{3+} for Si^{4+} and octahedral Fe^{3+} and Mg^{2+} for Al^{3+} substitutions were calculated, as well as general interatomic measurements including vacancy site dimensions, K-O distances, location of K ion and basal surface corrugations plus XRPD patterns. The study presented here focuses on four different types of illite particles with $2M_1$ characteristics, each with the same structure, but varying in their interlayer molecules, containing either ammonium (NH_4^+) or hydronium (H_3O^+) as well as potassium (K^+) ions, or two different proportions of water as well as K^+ ions. The following Sections describe their construction, computational methodology and analysis of the lattice parameters, together with an examination of the positions of the interlayer molecules, IR frequencies and simulated XRPD patterns.

MODELS

The crystal structure of the $2M_1$ illite identified by Gualtieri (2000) was used as the template structure in our study, from which we built four illite particle models containing different interlayer molecules. The particle model was made by increasing Gualtieri's *c*-length by half, which enabled the creation of two interlayer spaces, with each layer rotated 120° with respect to one another as shown in Figure 1. If the periodic crystal structure of Gualtieri (containing two clay layers) is representative of a single, $2M_1$, infinitely sized crystal of illite, then the inclusion of a third clay layer plus vacuum space in our models effectively simulates a truncated (1.5 x unit cell) 'particle' of illite bearing characteristics of the parent, $2M_1$ polytype. Within the context of gas shale, where mixed stacks of illite (I and I-I) and smectite (I-S) are found, modeling a 1.5-sized particle of illite is reasonable. From this point onwards the label 'pfb-$2M_1$' means 'particles from bulk illite bearing characteristics of $2M_1$' to distinguish it from purely crystalline $2M_1$ illite.

The inclusion of a third layer also means that the relaxed models are ready for use in further studies concerning interfaces, requiring only the addition of extra vacuum space above the top (or below the bottom) layer. The artificial electrostatics created between the topmost and bottommost basal sheets on addition of vacuum space, are minimal due to the similar electron densities of the basal sheets. We found that increasing the vacuum space from approximately 4 to 20 $\mathring{A}$ in the models with a bottommost siloxane sheet and topmost siloxane with an Al substitution, i.e., NH_4^+, H_3O^+ and 2I-H_2O, produces a maximum energy increase of 8 meV/atom, which suggests a weak dipole interaction, and in the model with an upper and lower siloxane sheet (I-H_2O) the energy decreases by 0.1 meV/atom, suggesting a negligible Coulomb interaction. The strength of a dipole interaction between periodic images separated by vacuum space, (an artifact of the modeling method) initially increases on increasing the vacuum space, therefore, maintaining a small vacuum space reduces its effect on the results, although the aforementioned energy differences suggest its effect would be minimal. Although the Coulomb interaction is decreased on increasing the vacuum space, the difference in energy is negligible and not worth the extra computational expense. Therefore, for all models we chose the smaller vacuum space (of 4 $\mathring{A}$) as illustrated in Figure 1.

Gualtieri's original crystal structure did not contain any Fe, Mg atoms and the substitutions of Al^{3+} for Si^{4+} in the tetrahedral sheets were numerous. To create a model that more closely fits the general formula for $2M_1$ illite, two octahedral substitutions were made, Fe and Mg for Al and the Al/Si substitutions were decreased in number. The optimum positions of these substitutions in identical clay layers, are the focus of our concurrent study on $1M$ polytypes, (Geatches and Wilcox, 2013) the results of which have been used in this study to fix the two octahedral and various tetrahedral substitutions. The pfb-$2M_1$ models represent fragments of samples of illite such that each fragment is a neutral unit in its entirety, and the general formula of the models is based on $K_{1.67}(Al_{3.29}Fe_{0.38}Mg_{0.32})[(Si_{6.68}\ Al_{1.32})O_{20}(OH)_4]$.

Four main varieties of pfb-$2M_1$ were made, one labelled 'NH_4^+' with two ammonium ions substituted for two K^+ ions in the same interlayer, as reported in Nieto (2002); one labelled 'H_3O^+' with a single hydronium ion substituted for a K^+ ion in the same interlayer; one labelled '2I-H_2O' with two water molecules inserted, one in each interlayer space as many illite formulae contain about 0.42 molecules of water per unit of $O_{10}(OH)_2$; and the fourth variety labelled 'I-H_2O' contains only one water molecule substituted for a K^+ ion. These latter two models are based on Hower's and Mowatt's (1966) postulate that interlayer, molecular water exists in illite as well as in the form of water lenses. To compensate for the reduced interlayer charge on the substitution of a K^+ ion by a molecule of water, there is no Al for Si substitution in the tetrahedral sheet of the layer containing the octahedral Mg - see Figure 1. Although this produced a lower proportion of K^+ ions in this model, it was necessary in order to balance the layer and interlayer charges. The composition of the three layers of the NH_4^+, H_3O^+ and 2I-H_2O models are identical, and the I-H_2O model differs only in its topmost layer, where there is no tetrahedral substitution of Al^{3+}

for Si^{4+}. The NH_4^+ illite investigated in our study is distinguished from tobelite by having an equivalent number of NH_4^+ and K^+ ions, (tobelite has more NH_4^+) which falls within the range 30 to 59% found by Nieto (2002) for shales (associated with coal seams). The positioning of both NH_4^+ ions in the same interlayer rather than distributed between interlayers, is based on the previous studies by Drits et al. (1997) and Nieto (2002).

Table 1 summarizes the relative proportions of the different atoms in all of the models made in this study and compares them with the general formulae of illite, $2M_1$ polytypes. All data in this study are provided without standard deviation values. Generally speaking, quantum chemistry/physics codes do not produce them because in theory, the ground state for a particular structure should always be the same. Analogous computational standard deviation values are contained within the convergence criteria, which effectively describe the precision of the calculations, thus enabling reproducibility. These criteria are described in detail in the following section.

COMPUTATIONAL DETAILS

All calculations were performed using the DFT code, CASTEP (Clark et al. 2005), using a plane wave basis set and pseudo potentials within the DFT formalism (Kohn and Sham 1965a; 1965b; Payne et al. 1992). The valence electron wave functions were expanded in a plane wave basis set represented by a kinetic energy cut-off of 500 eV, which gave an energy difference in total energies of less than 0.5 meV per atom for higher cut-offs. The electron-ion interactions were described by PBE ultrasoft pseudopotentials (Vanderbilt 1990) and for Fe, this included core corrections (Louie et al. 1982). These were consistent with the description of the exchange-correlation effects by the generalized gradient approximation (GGA) density functional, specifically Perdew, Burke and Ernzerhof (PBE) (Perdew et al. 1996), which describes molecular bonding to a greater accuracy than does the local density approximation (LDA). The (geometry) optimizer was Broyden-Fletcher-Goldfarb-Shanno (BFGS) (Pfrommer et al. 1997) and the electronic method was ensemble density functional theory (EDFT) (Mazari et al. 1997). The Brillouin zone integrations were performed on a Monkhurst Pack, (Monkhurst and Pack 1976) 2 x 2 x 1 grid as this gave convergence to within the error bound just described. Further convergence details per BFGS iteration are as follows:- energy change per ion: dE/ion 2x10^{-5} eV; electronic energy tolerance: 10^{-8} eV; maximum force: |F|max 0.05 eV/$\mathring{A}$; change in displacement: |dR| 0.002$\mathring{A}$. All calculations were spin polarized and all models were created and visualized using Materials Studio (Accelrys 2012). All lattice parameters and atomic coordinates were allowed to relax to equilibrium (unless otherwise stated) within the convergence criteria previously stated.

The vibrational frequency calculations were carried out on the fully relaxed structures of the ammonium, hydronium and the I-H_2O model, using the method of finite displacement (Frank et al. 1995). This method could not be applied to the 2I-H_2O model, because although it converged to a force tolerance of the order of 10^{-2} eV/$\mathring{A}$ within the same time interval as the other computations, this value was not sufficiently low to obtain reasonable phonon frequencies.

Materials containing strongly correlated electrons of the transition metals can prove problematic when addressed with density functional theory and there is no consensus on their optimum treatment. Some systems produce results closer to experiment when the d- and f-electrons are not explicitly treated, whereas others produce spurious results if they are not. The Hubbard (or 'U') value is an energy term that is added to the system such that it creates repulsion between, in this case, the d-electrons of Fe, thus reducing their strong correlations and consequently the artificially high electron density on Fe. Theoretical details can be found in Anisimov et al. (1997) and Mosey and Carter (2007), and an example of its implementation in Zhou (2004). In our concurrent study of $1M$ illites we determined a Hubbard value for the Fe in identical, component clay layers. As there is no experimental band-gap data available to use as a guide to determining the correct Hubbard value, we used other means such as examining the relative shift of the valence band of the p-electrons of the tetrahedral Al; the energy-width separation of d-orbitals of Fe; the change in the band gap of Fe-illite and the location of Fermi level orbitals, all with different U-values. The analysis resulted in an optimum Hubbard parameter of 4.5eV, and it is this value that is used throughout this study for all Fe ions. Further details of this analysis can be found in the Supplementary Material of the concurrent study at, http://eurjmin.geoscienceworld.org/.

Simulated, X-ray powder diffraction (XRPD) patterns were created using the Reflex module of Materials Studio (Accelrys 2012). The simulated radiation sources were Cuα_1 and Cuα_2; the diffractometer range was 2-theta from 5° to 70°; the temperature factor was atomic and the line shift Bragg-Brentano. There was no asymmetry correction applied nor any lattice strain. On the resulting simulated XRPD patterns, the major peaks up to 30° have been assigned their corresponding $(h\ k\ l)$ labels.

RESULTS AND DISCUSSION

General formula

Considering the small size of the illite models created in this study, there is generally good agreement between their formula ratios and those listed from experimental data -see Table 1. Experimentally, the interlayer molecule (I-M) ratios vary from 0.56 to 0.84, compared to the simulated ratios of 0.33 to 0.67, and those for the K^+ ions vary experimentally from 0.84 to 1.40 compared to the models varying from 0.67 to 1.33. The upper limit for the K^+ ions is achieved in the 2I-H_2O models. For the tetrahedral sheet the proportion of Si varies experimentally from 6.68 to 6.88, and in the models from 7.00 to 7.33; the experimental range for Al is from 1.12 to 1.32 and the simulated, from 0.67 to 1.00. This suggests that there could be too much Si and insufficient Al in the simulated models, although changing the ratio in favor of increasing Al would require an increase in the number of charged interlayer molecules. There is potential for the insertion of additional, non-K^+ ion interlayer molecules, but all except the K^+ ion ratio of the NH_4^+ model already fall within the experimental range cited. The octahedral sheet cations range experimentally from 0.38 to 0.50 for Fe; from 2.94 to 3.29 for Al, and from 0.32 to 0.56 for Mg; whereas the simulated ratios are 0.33, 3.33 and 0.33, respectively. The closest agreement for the ratios in the octahedral sheet between the models and experiment, is in the

NH_4^+ illite, but this same model diverges from the experimental ratios in its tetrahedral sheet and interlayer species. Conversely, the 2I-H_2O model agrees closest with the experimental data in the interlayer species, and diverges in its tetrahedral and octahedral sheets. The overall conclusion from these simulated model ratios when compared to the selection of experimental data, must be that, given their constrained size, there is no evidence to suggest that they are not representative of physical, $2M_1$ illite particles.

Lattice parameters

The relaxed configurations of the pfb-$2M_1$ models are shown in Figure 1, and their lattice parameters in Table 2, together with experimental results originating from a different source other than that used to create the parent pfb-$2M_1$ illite. It is difficult to compare the parameters of the NH_4^+ model with experimental data because the ammonium molecule is difficult to detect and could be missed if not specifically looked for. This means that NH_4^+ could exist in any generic specimen of $2M_1$ illite, without recognition. The experimental c-length provided in Table 2 is based on refined XRD data, assuming that each interlayer of the specimen contains either NH_4^+ or K^+, and these have corresponding lengths of 10.33 $\AA$ and 9.98 $\AA$, respectively. If we assume that the remaining parameters of the experimental sample (in Table 2) are represented by those reported by Nieto et al. (2010), and we compare these with our NH_4^+ model, then we can say that the a- and b-lengths agree with experiment to within the expected 1%, (allowing for the GGA exchange-correlation functional) as does the γ-angle. The c-length varies from experiment by 1.8%, the α-angle by 1.3%, and the β-angle by 2.2%.

For the H_3O^+ model, the deviation from experimental data for all lattice parameters is less than 1%. For the 2I-H_2O model — containing two interlayer molecules of water — the lattice parameters were fixed at Gualtieri's experimentally obtained values given in Figure 1. This was done after a full relaxation was attempted, which resulted in an α-angle of 82°, and a β-angle of 99°, both suggesting an unrealistically large effect on the illite structure produced by two water molecules. Further analysis showed that both water molecules were oriented with their hydrogen atoms bound to both upper and lower clay layers, which enabled the unit cell to shear in both the x- and y- directions and to increase in the z- direction to reduce the internal stresses. Within a fixed lattice, the internal stresses were reduced by the water molecules reorienting themselves to lie more horizontally within the interlayer space, with one water molecule attached by hydrogen bonds to the upper clay layer only. The theoretical results for 2I-H_2O agree with the experimental results (of researchers other than Gualtieri) to within 1% for all lattice parameters except the b-length, which differs by 1.8% and the c-length by 4.3%. This latter discrepancy with experiment is of little concern given that the lattice parameters were fixed for this model. For the I-H_2O model — containing a single water molecule substituting a K^+ ion — the agreement is within 1% for all lattice parameters, and this model was allowed to fully relax.

The agreement between our models and experimental data is close, deviating little from the minimum 1% expected by using the GGA exchange-correlation functional, which suggests the lack of inclusion of van der Waals forces has had no significant impact on the final structures.

Comparing the depths of the layers of the NH_4^+ models, it can be seen that the theoretical values mirror the experimental data, in that the layers containing only NH_4^+ ions are larger than those containing K^+ ions. The simulated layer depth for the former is 2% larger than experiment and that for the latter, 1.5% larger. The average of the simulated depths for these two layers, is 10.33 $\AA$, which exactly matches the cited depth for NH_4^+.

Experimental data for H_3O^+, I-H_2O and 2I-H_2O is lacking so it is impossible to comment on their layer depth deviations from physical illite samples. However, we can observe from the model results that the difference between the layer depths is less for the H_3O^+ illite, which is not surprising considering it had only one H_3O^+ ion. The layer depth containing a single H_3O^+ ion is about the same as that containing a single water molecule in I-H_2O, an unsurprising observation given the similarity of the two interlayer molecules.

The 2I-H_2O model has a single water molecule in each layer and the layer depths are the same. For model I-H_2O, the layer containing the water molecule is larger than the layer containing K^+ ions only. The layer depth of NH_4^+ is 3% larger than that containing a K^+ and H_3O^+ ion, and 3.5% larger than that containing a water molecule and a single K^+ ion, and 0.9% larger than that containing two K^+ ions plus a water molecule. The smaller difference between NH_4^+ illite and 2I-H_2O suggests that, based on layer-depths alone, these two types of illite might be indistinguishable, whereas the percentage differences between NH_4^+, H_3O^+ and I-H_2O illite are generally larger than the percentage deviation from experiment, which suggests that the simulated results are representing a trend that could be detectable experimentally. If so, then such an experimentally-obtained trend could, when compared to our simulated trend, help identify the interlayer molecules within $2M_1$ illite.

Interlayer molecule location

Figure 2 shows the relative positions of the interlayer molecules with respect to the immediate lower and upper clay layers and the siloxane and Al/siloxane cavities, as well as side views of the interlayer space to illustrate the corrugations. Table 3 records the minimum and maximum internal angles of the two distinct siloxane and Al/siloxane rings or cavities for each of the interlayer spaces (top -‘t’ and bottom -‘b’) projected onto the lower (‘l’) and upper (‘u’) clay layers. Throughout this section the reader is referred to the aforementioned Figure 2 and Table 3.

The bottom interlayer environment of NH_4^+ and H_3O^+ as experienced by the two K^+ ions is almost identical, which is confirmed by the angles listed under ‘b-l’ and ‘b-u’ in Table 3, varying between models by an average of less than 1% and falling in the range from 108° to 131°. The agreement between these two types of illite is expected due to the identical bottom interlayer molecules, which suggests that the top interlayer environment experienced by the K^+ ions of the I-H_2O illite, might share the same appearance and angle measurements. This is not the case, however, as the t-l rings show a greater deviation from regular hexagons, with angles varying from 91° to 147° and the t-u rings are closer to hexagonal with internal angles of

116° to 123°.

The bottom interlayer environment of I-H_2O occupied by a water molecule and K^+ ion, displays rings that deviate from regular hexagonal, with internal angles between 99° to 138° in the lower clay layer, and 108° to 132° in the b-u sheet. For the 2I-H_2O illite, the deviation is less, with internal angles from 112° to 127° in the b-l sheet and from 114° to 126° in the b-u sheet. In I-H_2O where a K^+ ion has been substituted by a water molecule, it is positioned centrally within the cavity, oriented so that both hydrogen atoms are hydrogen-bonded to two alternate oxygens around the Al in the b-l sheet. In the 2I-H_2O illite, the water is additional to the K^+ ions, which has resulted in a translation of the middle clay layer with respect to the lower clay layer. One of the K^+ ions in the bottom interlayer lies centrally in the lower cavity, while the second K^+ ion is displaced off-center with one hydrogen atom of the water molecule hydrogen-bonded to an oxygen close to the Al substitution in the b-l sheet, and the second hydrogen forms two hydrogen bonds with adjacent oxygen atoms in the b-u sheet. The water molecule is thus hydrogen-bonded to both clay layers. Relative to the b-u sheet, the water molecule lies central in the same cavity with a displaced K^+ ion, and the second K^+ ion lies in an identical position in its own cavity.

An examination of the interlayer environment containing the two NH_4^+ ions, reveals the internal angles of the hexagonal cavities in the t-l sheet range from 85° to 152°, and those in the t-u sheet from 116° to 124°, with the NH_4^+ ions lying central to both rings. All four hydrogen atoms of each NH_4^+ ion are hydrogen-bonded to the clay layers, with three hydrogen atoms bonded to oxygens in the t-u sheet and one to an oxygen atom close to the Al substitution in the t-l sheet. The hydrogen bonds formed are between 1.84 $\AA$ and 2.50 $\AA$ in length.

In the H_3O^+ illites, the internal angles of the hexagonal cavities in the t-l sheet lie between 86° to 151°, and in the t-u sheet, between 107° to 133°. With respect to the t-l sheet, the H_3O^+ ions and K^+ ions are not central, but they are positioned identically within the cavity. With respect to the t-u sheet, they are both central in the cavity, although the cavity itself is skewed. The H_3O^+ ion is hydrogen-bonded to both clay layers, forming two H-bonds with opposite oxygens of the upper sheet and one H-bond with an oxygen close to the Al substitution of the lower sheet. All three hydrogen bonds are about the same length, 1.66 $\AA$, 1.64 $\AA$ and 1.70 $\AA$.

In the I-H_2O illite, the internal angles of the cavities in the t-l sheet lie between 91° to 147°, and those in the t-u sheet, between 116° and 123°, and the K^+ ions lie almost centrally in the former case and centrally in the latter. The water molecule has formed two hydrogen bonds of 2.03 $\AA$ and 1.95 $\AA$ between its hydrogen atoms and the oxygen atoms of the lower clay layer.

In the 2I-H_2O illite, the internal angles of the cavities in the t-l sheet lie between 88° to 151°, and those in the t-u sheet, lie between 113° to 127°. Both water molecules have formed hydrogen bonds between their hydrogen atoms and the oxygen atoms of adjacent clay layers ranging in length from 1.65 $\AA$ to 2.42 $\AA$. The positions of the interlayer species varies, with K^+ ions lying central in one cavity of the t-l sheet, and where a K^+ ion occupies the same cavity as a water molecule, the K^+ ion is displaced to one corner and the water molecule lies above an SiO_3 ring such that it is oriented towards the edge of an upper SiO_3 ring, to which it is hydrogen-bonded.

With respect to the t-u sheet, one K^+ ion lies centrally in the cavity, whereas the occupation of the second by a K^+ ion and water molecule causes a displacement of both from the central position. In the upper interlayer space the distances between the oxygen atom of the water molecule and the K^+ ions is 4.22 $\AA$ and 3.70 $\AA$, and in the lower layer the comparable distances are 3.87 $\AA$ and 2.46 $\AA$. This is much shorter than the 5.66 $\AA$, K^+ - O distance in I-H_2O, which is to be expected given that there are two more molecules in 2I-H_2O than I-H_2O.

Considering the b-s and t-s views, there is little difference in the degree of corrugation of the interlayer edges; the interlayer species in the bottom interlayer space lies closer to the lower clay layer, apart from the water molecules of 2I-H_2O, which lie closer to the middle clay layer. The positions of the interlayer species is more varied in the top interlayer space, where the NH_4^+, H_3O^+ and associated K^+ ions lie closer to the top clay layer, and the K^+ ions of I-H_2O lie centrally in the interlayer space, and the positions are mixed in the I-H_2O illite.

The previous analysis leads to the assertion that the shape of the tetrahedral cavities including an Al substitution, is governed principally by the octahedral sheet substitutions within the same clay layer, and that the interlayer species has a lesser effect on cavity geometry. We assert this because the consistency of the clay layers between models matches the consistency in the ranges of the internal angles of the hexagonal cavities, within the b-l, b-u, t-l and t-u groups for NH_4^+, H_3O^+ and I-H_2O, (the 2I-H_2O model was not allowed to relax so has not been included) whereas the type of interlayer molecules within each interlayer space differs. Also, the t-l groups for all three models have the largest range of internal, hexagonal cavity angles and each of the corresponding clay layers (the middle layer) has an all-Al octahedral sheet, whereas the interlayer molecules differ across the models. Our assertion is analogous to the findings of Drits et al. (2010) on 1*M* mica, where they show that the relative Al/Mg/Fe octahedral occupation determines the basal surface corrugation of the tetrahedral sheet, i.e., both their analysis and ours show that the octahedral sheet environment affects the shape of that of the tetrahedral sheet.

When considering the all-Si cavities, (the 'Si' column under '5Si-Al/Si' in Table 3) there seems to be a secondary effect on the internal angles of these hexagonal cavities, directly related to their relative occupation, i.e., whether they are identically occupied by the same species. The evidence for this comes from the t-u range in H_3O^+ and the b-u range in I-H_2O, which are larger than all other Si-only cavities, and these differ from other occupations by having two different species in the same interlayer space. Although 2I-H_2O also has two different species, the unit cell was not allowed to relax, even so, its all-Si cavities have a slightly larger range than the same-species, (t-u) all-Si cavities of NH_4^+ and I-H_2O and a smaller range than those encasing two K^+ ions (b-u) of NH_4^+ and H_3O^+. The order in decreasing range of the internal angles of the fully relaxed models is: two different ions $>$ two K^+ ions $\geq$ two NH_4^+ ions. The skewing of the all-Si cavity in the t-u sheet of H_3O^+ appears to be due to the asymmetrical hydrogen bonding, which might have been evident in the 2I-H_2O model also, had the lattice been allowed to relax. Given that the relative strength of a hydrogen bond is inversely proportional to its length, then we can say that the strongest hydrogen bonds were formed by the H_3O^+ ion, followed by the water molecules in 2I-H_2O, and I-H_2O followed by the NH_4^+ ion. This skewing effect might play a role in the process of metamorphism within clay mineral layers, where the presence of interlayer molecules creates strain on the hexagonal cavities, which, under temperature and pressure leads to metamorphic change.

In summary, the deviation of the cavities from regular hexagons with internal angles of 120°, is determined for the all-Si cavities by the species occupying neighboring hexagons, i.e., where these species are the same, the all-Si cavities will be more regular than where these neighboring species are different. For the Al/Si cavities, their deviation from regular hexagons is determined by the octahedral sheet substitution, e.g., an Fe-for-Al^{3+} substitution in an otherwise all-Al octahedral sheet has a larger effect on the internal angle range than no substitution. If the shape of these cavities were experimentally accessible, then these theoretical results would enable characterization of the type of illite in a physical sample.

Vibrational Frequencies

The simulated infrared frequencies of the interlayer molecules of the three pfb-$2M_1$ illites, NH_4^+, H_3O^+ and I-H_2O are shown in Table 4, together with descriptions of their motions. The frequencies displayed are those of the interlayer molecules only. There are more frequencies where the interlayer molecules are vibrating in conjunction with the clay mineral, but this type of vibration would be less viable in the physical sample due to the constraints of the bulk of the material. All vibrational frequency calculations produced several imaginary frequencies, which could be interpreted as indicative of mechanical instability, and also an artifact of the spectroscopic method applied to these artificially homogeneous materials. Linear response theory in the form of density functional perturbation theory (DFPT) (Gonze 1997; Refson et al. 2006) would be the preferred method, but unfortunately the content of the models excluded it from this type of calculation. Inaccuracies in calculated frequencies originate from poorly converged relaxations and are most likely to affect lower wave numbers. The relaxations in this study were well-converged, and, given that the measured IR frequencies for these illites have wave numbers above 1000 cm^{-1}, we can confidently present the frequencies as being worthy of comparison with experimental data.

Considering NH_4^+ illite, the frequencies between 1392 cm^{-1} and 1666 cm^{-1} are all either scissoring, wagging or rocking modes or a combination of any two or all three, whereas the frequencies from 3172 cm^{-1} to 3552 cm^{-1} are all stretching, either symmetric or antisymmetric or combinations of the two. The work of Juster et al. (1987) concerning tobelites, and NH_4^+ cations being their principle identification feature, proposed IR absorption bands at 1430 cm^{-1} and 3000-3400 cm^{-1}, which is in agreement with the results presented here. Bobos (2012) in agreement with Higashi (1982), found four N-H stretching and bending frequencies in NH_4-illite at 1430, 2834, 3060 and 3326 cm^{-1}, with the characteristic bending and stretching modes at 1430 cm^{-1} and 3330 cm^{-1} respectively, which closely match the simulated wagging/bending and stretching at 1427 cm^{-1} and 3338 cm^{-1} respectively.

The simulated IR frequencies for the H_3O^+ ion within H_3O^+ illite shown in Table 4, record that the vibrations at 1576 cm^{-1} and 1668 cm^{-1} are scissoring motions, 2747 cm^{-1} is an anti-symmetric stretch; 2854 cm^{-1} is a symmetric stretch and 3110 cm^{-1} is stretching of a single OH group. Yeh et al. (1989) report calculated and theoretical IR frequencies of anti-symmetric and symmetric stretches at 2660 cm^{-1} and 3000 cm^{-1}, respectively, for a H_3O^+ ion within a hydrated hydronium cluster. These values are not particularly close to our simulated anti-symmetric and symmetric stretches at 2747 cm^{-1} and 2854 cm^{-1}, respectively, but Yeh et al.'s symmetric stretch is close to that found at 2600 cm^{-1} by Cicero et al. (2008) who carried out a first-principles investigation of water confined in nanotubes. An IR investigation of the interaction between hydronium ions and OH groups in a montmorillonite (Russell and Fraser 1970) showed absorption bands at 1700 cm^{-1} and 2900 cm^{-1}, which are very close to the simulated 1668 cm^{-1} and 2854 cm^{-1} seen in this study. The absorption bands found in the former IR investigation, agreed with those found much earlier by Falk and Giguère (1957) in the aqueous phase of H_3O^+, and the frequency at 2900 cm^{-1} has been subsequently explained as "..the stretching vibration of OH groups in hydrogen bridges..." and both frequencies (plus a third at 1200 cm^{-1} found by Falk and Giguère 1957) were explained to be due to solvation effects (Grahn 1962). Begemann et al. (1983) and Begemann and Saykally (1985) detected hydronium in the gas phase at IR frequencies of 3513/3519 cm^{-1} and 3530/3536 cm^{-1} for the v_3 mode or doubly-degenerate asymmetric stretch, and Haese and Oka (1983) found IR frequencies for the v_2 mode between 1000 to 1200 cm^{-1}, all of which has been confirmed by Colvin et al. (1983) with theoretical calculations of v_1, v_2 and v_3 frequencies at 3396, 814 and 3500 cm^{-1} respectively.

The simulated IR frequencies of the water molecule in I-H_2O illite, given in Table 4, show that 1640 cm^{-1} is a scissoring mode, 3651 cm^{-1} a symmetric stretch and 3708 cm^{-1} an anti-symmetric stretch, all of which relatively closely match the recorded gas-phase vibrations of H_2O (Shimanouchi 1972) at 1595 cm^{-1} ('bending'), 3657 cm^{-1} ('symmetric stretch') and 3756 cm^{-1} ('anti-symmetric stretch') respectively. The simulated frequencies for NH_4^+ illite match the experimental data very well, which is to be expected as the experimental data is from illite-containing NH_4^+, i.e., the sources of the IR frequencies are comparable. The relatively close match between the simulated and experimental IR frequencies for the water molecule in I-H_2O illite is also understandable as their sources are similar. The model contains an isolated water molecule, simulating a gas-like phase. The similarity in IR frequencies between simulation and experiment for these two types of pfb-$2M_1$ illite lends confidence to the robustness of the method, that is, employing DFPT, had it been possible, might have brought these frequencies closer, but the finite difference method employed has produced reasonable results. Therefore, the dissimilarities found in the H_3O^+ illite between simulation and experiment is originating elsewhere than the methodology. The H_3O^+ model contains a gas-like phase of a hydronium ion, but its frequencies match those originally believed to be of its aqueous phase, which were subsequently described as not being specifically attributable to hydronium. Perhaps the simulated frequencies are affected by the hydrogen-bonding between the hydronium and the clay layers, which is more representative of an aqueous environment, with the hydronium behaving like a solvated proton. Perhaps the similarity in frequencies found by Cicero et al. and Yeh et al. when investigating water (in a confined space) and hydronium (hydrated clusters) respectively, illustrates the inherent difficulties involved in experimentally distinguishing between these species. Our results and their dissimilarities to available experimental data, infer agreement with Cicero et al.'s assertion that the confining environment affects the rearrangement of the electronic structure of the confined medium. Therefore, without any further IR spectroscopic data of a hydronium ion in a clay-layered environment, it is futile to speculate further on the origins of the disagreement between the existing experimental data and our simulated frequencies. Such a comparison must be postponed until experimental data from a similar environment has been produced.

If we assume that the simulated frequencies are state-of-the-art for these types of heterogeneous materials, then it can be stated that each type of illite has produced unique IR frequencies, which could contribute to the identification of their physical analogues in, for example, samples of gas-bearing shale.

X-ray powder diffraction (XRPD) patterns

The XRPD patterns shown in Figure 3 have been simulated from pure crystals and consequently display very well defined reflection peaks. Drits et al. (1997) examined the amount and distribution of ammonium in illite-smectite by using a peak-profile fitting program that, based on the XRD spectra, (d_{002}, d_{005} and full-width at half-height values -FWHH) produced various illite structures containing either mixed K/NH_4 interlayers or separate K and NH_4 interlayers. They produced two sets of ratios FWHH(005)/FWHH(002) for these two types of configurations of ammonium in illite-smectite. This ratio (shown in Table 5) scaled for our simulated 3-layer models for separate K and NH_4 interlayers is 1.45, which agrees very well with Drits et al.'s ratio of 1.43 for their separate layered, 50% NH_4 content. Our XRPD data gives a lower value for the average d_{00l} spacing compared to theirs, which could be due to the larger numbers of layers they used, and also that we created a truncated crystal, which would have a slightly smaller average of cations per layer compared to bulk crystal.

Nieto (2002) reported that the NH_4 content of micas could be detected by the position of the (005) peak or d_{005} according to Juster et al. (1987), Sucha et al.(1994) and Higashi (2000), where the (005) reflection informs the mean basal spacing. The equivalent reflection peak for our 3-layer models is (0015) and is recorded on all four simulated XRPD spectra, which may be of some significance in spite of its low intensity. Table 5 shows the mean basal d_{003} spacing for all of our four models, together with their corresponding 2θ peaks, and although the differences between the values in each set are small, both sets show the trends predicted by Drits et al. (1997) vis, for interlayer species other than K^+ ions, as the basal spacing increases, the corresponding 2θ angles shift to smaller values.

Liang and Hawthorne (1996) used XRPD spectra and Rietveld refinement techniques of an illite sample consisting largely of $2M_1$, $1M$ and minor quartz to determine whether hydronium ions do exist as K^+ ion substitutes. One of their refined spectra shows observed peaks with relative intensities at 2θ of the order 35 <19 <27 as does the simulated spectra for H_3O^+ illite shown in Figure 3. This trend also appears in the simulated NH_4^+ illite spectrum, but not in those of I-H_2O nor 2 I-H_2O, which could be a feature that helps distinguish between hydronium- and water- bearing illites, although the reality is that the former will almost certainly contain the latter. Comparisons between spectra show there are a few peak intensity differences between NH_4^+ and H_3O^+ illites, which may be identifiable in the XRPD patterns of physical samples. The two models containing water, I-H_2O and 2I-H_2O, show a slightly increased intensity peak for the (002) reflection, compared to the two models without water, and there are some differences in peak intensities between the two water-bearing models. The XRPD pattern for all four models has essentially the same structure, which is to be expected as their clay mineral layers are identical, apart from the topmost tetrahedral sheet of I-H_2O, which is all-Si, i.e., the Al substitution is absent. In Figure 4 the XRD patterns calculated from the molecular modeled structures are compared with an XRD pattern calculated for a trans vacant $2M_1$ mica having an iron free composition of $K_{0.8}(Al_{0.8}Si_{3.2})(Al_2)O_{10}(OH)_2$, and orthogonal unit cell parameters of a = $5.21 Å$, b = $9.03 Å$, c = $9.99 Å$, $\gamma = 90°$ and an intralayer X translation of -0.4022 (Drits and Tchoubar, 1990). The *hkl* indices shown are based on a monoclinic C2/c unit cell.

Combining the aforementioned analyses of lattice parameters, positions of interlayer molecules and shapes of hexagonal, siloxane-based cavities, together with the infrared frequencies and XRPD data, could in theory help distinguish between $2M_1$ illites with varying interlayer molecules. For example, a sample exhibiting an average layer depth of between 10.30 to 10.50 Å, together with an absence of IR frequencies at 1430 cm^{-1} and 3000-3400 cm^{-1}, and exhibiting an XRPD pattern without the 2θ ratio of the order 35 <19 <27 is probably, based on the analysis within this study, an illite containing K^+ ions and water molecules within its interlayers, resembling the 2I-H_2O model. Distinguishing an ammonium illite is simpler due to the marked IR frequencies of NH_4, whereas a hydronium illite requires further evidence, which, if the shape of the siloxane cavities could be identified, would reveal a unique, (within the context of this study) skewed shape.

IMPLICATIONS

We have shown that the four varieties of illite particles with $2M_1$ characteristics and interlayer ions of K^+ and either, NH_4^+, H_3O^+, or two different concentrations of H_2O, are all feasible models of illite particles within gas shale, based on the available experimental and crystallographic data, and each have characteristics that suggest they would be distinguishable in a physical sample. The creation and validation of these illite structures is the first step on the research path to understanding how these varieties of illite might influence the extraction and enhanced recovery of CH_4 from gas shale, and the long-term storage of sequestered CO_2 within the exhausted shale beds. For example, in shale, CH_4 and CO_2 could occupy the external surfaces of one or all of these varieties of illite. The models we have created could be used as templates from which to build basal surfaces, (by the addition of extra vacuum space) as well as the potentially more reactive edges (by cleaving along [010] and [110] planes). Ab initio investigations involving such surfaces would determine whether CH_4 and CO_2 reacted with these surfaces chemically, or electrostatically, or perhaps both. This information and these models could be used to feed into larger scale modeling such as molecular dynamics, as well as to support and inform experimental results. Such a synergistic relationship between modeling and experiment, will contribute to a thorough and rigorous atomistic-scale investigation of illite and its interactions with CH_4 and CO_2, leading to a deeper understanding of the nature of these interactions within a shale environment. In the hope of accelerating this process, we have provided the four varieties of the relaxed illite structures as .cif files in the Supplementary Material.

ACKNOWLEDGEMENTS

We would like to acknowledge the high performance computing (HPC) facilities in the Center for Computational Earth and Environmental Science (CEES) at Stanford University, and the Texas Advanced Computing Center (TACC), at the University of Texas at Austin for providing HPC resources that have contributed to the research results reported within this paper: URL: http://www.tacc.utexas.edu. Our appreciation is also extended to the developers of the CASTEP code for their support, to Cindy Ross and Gordon Brown for their helpful input, to BP for their financial support during the course of this research, and finally to the anonymous reviewers whose helpful comments improved the presentation of our work.

References

Accelrys (2012) Materials Studio. Modeling and Simulation Software.

Anisimov, V.I., Aryasetiawan, F., and Lichtenstein, A.I. (1997) First-principles calculations of the electronic structure and spectra of strongly correlated systems: The LDA+U method. Journal of Physics-Condensed Matter, 9, 767-808.

Begemann, M.H. and Saykally, J.R. (1985) A study of the structure and dynamics of the hydronium ion by high resolution infrared laser spectroscopy. I. The v_3 band of $H_3{}^{16}0^+$. Journal of Chemical Physics, 82, 3570-3579.

Begemann, M.H., and Gudeman, C.S., Pfaff, J., and Saykally, J.R. (1983) Detection of the hydronium ion (H_3O^+) by high-resolution infrared spectroscopy. Physical Review Letters, 51, 554-557.

Bobos, I. (2012) Characterization of smectite to NH_4-illite conversion series in the fossil hydrothermal system of Harghita Bãi, East Carpathian, Romania. American Mineralogist, 97, 962-982.

Brown, G. and Norrish, K. (1952) Hydrous micas. Mineralogical Magazine, 29, 929-932.

Cicero, G., Grossman, J.C., Schwegler, E., Gygi, F., and Galli, G. (2008) Water confined in nanotubes and between graphene sheets: A first principles study. American Chemical Society, 130, 1871-1878.

Clark, S.J., Segall, M.D., Pickard, C.J., Hasnip, P.J., Probert, M.I.J., Refson, K., and Payne, M.C. (2005) First principles methods using CASTEP. Zeitschrift für Kristallographie. 220, 567-570.

Colvin, M.E., Raine, G.P., and Schaefer, H.F. lll (1983) Infrared intensities of H_3O^+, H_2DO^+, and D_3O^+. Chemical Physics, 79, 1551-1552.

Drits, V. A., and Tchoubar, C. (1990) X-Ray Diffraction by Disordered Lamellar Structures. Springer, Verlag Berline Heidelberg.

Drits, V.A. and Zviagina, B.B. (2009) Trans-Vacant and Cis-Vacant 2:1 Layer Silicates: Structural Features, Identification, and Occurrence. Clays and Clay Minerals, 57, 405-415.

Drits, V.A., Lindgreen, H., and Salyn, A.L. (1997) Determination of the content and distribution of fixed ammonium in illite-smectite by X-ray diffraction: Application to North Sea illite-smectite. American Mineralogist, 82, 79-87.

Drits, V.A., Zviagina, B.B., McCarty, D.K., and Salyn, A.L. (2010) Factors responsible for crystal-chemical variations in the solid solutions from illite aluminoceladonite and from glauconite to celadonite. American Mineralogist, 95, 348-361.

Escamilla-Roa, E., Hernández-Laguna, A. and Sainz-Diaz, C.I. (2013): Cation arrangement in the octahedral and tetrahedral sheets of *cis*-vacant polymorph of dioctahedral 2:1 phyllosilicates by quantum mechanical calculations. *American Mineralogist*, **98**, 724-435.

Eslinger, E. and Pevear, D. (1988) Clay Minerals for Petroleum Geologists and Engineers. Society of Economic Paleontologists and Mineralogists, USA.

Falk, M. and Giguère P.A. (1957) Infrared spectrum of the H_3O^+ ion in aqueous solutions. Canadian Journal of Chemistry, 35, 1195-1204.

Fleet, M.E. (2003) Rock-Forming Minerals -Micas. (Second Edition), The Geological Society, Bath.

Frank, W., Elsässer, C., and Fähnle, M. (1995) Ab initio force-constant method for phonon dispersions in alkali metals. Physical Review Letters, 74, 1791-1794.

Geatches, D., and Wilcox, J. (2013) Ab initio investigations of dioctahedral interlayer-deficient mica: Modelling 1*M* polymorphs of illite found within gas shale. European Journal of Mineralogy DOI: 10.1127/0935-1221/2013/0025-2352.

Gonze, X. (1997) First-principles responses of solids to atomic displacements and homogeneous electric fields: Implementation of a conjugate-gradient algorithm. Physical Review B, 55, 10337-10354.

Grahn, R. (1962) Arkiv Fysik, 21.

Gualtieri, A.F. (2000) Accuracy of XRPD QPA using the combined Rietveld-RIR method. Journal of Applied Crystallography, 33, 267-278.

Haese N.N. and Oka, T. (1983) Observation of the v_2 ($1^- \leftarrow O^+$) inversion mode band in H_3O^+ by high resolution infrared spectroscopy. Journal of Chemical Physics, 80, 572-573.

Hernández-Laguna, H., Escamilla-Roa, E., Timón, V., Dove, M.T. and Sainz-Diaz, C.I. (2006): DFT study of the cation arrangements in the octahedral and tetrahedral sheets of dioctahedral 2:1 phyllosilicates. *Phys. Chem. Minerals*, **33**, 655-666.

Higashi, S. (1982) Tobelite, a new ammonium dioctahedral mica. Mineralogical Review, 11, 138-146.

Higashi, S. (2000) Ammonium-bearing mica and mica/smectite of several pottery stone and pyrophillite deposits in Japan: their mineralogical properties and utilization. Applied Clay Science, 16, 171-184.

Hower, J. and Mowatt, T.C. (1966) The mineralogy of illites and mixed-layer illite/montmorillonites. American Mineralogist, 51, 825-854.

Juster, T.C., Brown, P.E., and Bailey, S.W. (1987) NH_4-bearing illite in very low grade metamorphic rocks associated with coal, northeastern Pennsylvania. American Mineralogist, 72, 555-565.

Kohn, W. and Sham, L.J. (1965a) Quantum density oscillations in an inhomogeneous electron gas. Journal of Physical Review, 137, A1697-1705.

Kohn, W. and Sham, L.J. (1965b) Self-consistent equations including exchange and correlation effects. Physical Review, 140, A1133-A1138.

Lash, G.G. and Blood, D.R. (2004) Origin of shale fabric by mechanical compaction of flocculated clay: Evidence from the Upper Devonian Rhinestreet shale, western New York, USA. Journal of Sedimentary Research, 74, 110-116.

Lausen, S.K., Lindgreen, H., Jakobsen, H.J., and Nielsen, N.C. (1999) Solid-state Si-29 MAS NMR studies of illite and illite-smectite from shale. American Mineralogist, 84, 1433-1438.

Liang, J.J. and Hawthorne, F.C. (1996) Rietveld refinement of micaceous materials: Muscovite-$2M(1)$ a comparison with single-crystal structure refinement. Canadian Mineralogist, 34, 115-122.

Liming, J., Zhang, T., Milliken, K., Qu, J. and Zhang, X. (2012) Experimental investigation of main controls to methane adsorption in clay-rich rocks. Applied Geochemistry, 27, 2533-2545.

Lindgreen, H. (1991) Elemental and structural changes in illite/smectite mixed-layer clay minerals during diagenesis in Kimmeridgian-Volgian (-Ryazanian) clays in the Central Trough, North Sea and the Norwegian-Danish Basin. Bulletin of the Geological Society of Denmark, 39, 1-82.

Lindgreen, H., Garnaes, J., Hansen, P.L., Besenbacher, F., Laegsgaard, E., Stensgaard, I., Gould, S.A.C., and Hansma, P.K. (1991a) Ultrafine Particles of North-Sea Illite Smectite Clay-Minerals Investigated by STM and AFM. American Mineralogist, 76, 1218-1222.

Lindgreen, H., Jacobsen, H., and Jakobsen, H.J. (1991b) Diagenetic Structural Transformations in North-Sea Jurassic Illite/Smectite. Clays and Clay Minerals, 39, 54-69.

Louie, S.G., Froyen, S., and Cohen, M.L. (1982) Nonlinear ionic pseudopotentials in spin-density-functional calculations. Physical Review B, 26, 1738-1742.

Macht, F., Eusterhues, K., Pronk, G. J., and Totsche, K. U. (2011) Specific surface area of clay minerals: Comparison between atomic force microscopy measurements and bulk-gas (N_2) and -liquid (EGME) adsorption methods Applied Clay Science, 53, 20-26.

Mazari, N., Vanderbilt, D., and Payne, M.C. (1997) Ensemble density functional theory for ab initio molecular dynamics of metals and finite-temperature insulators. Physical Review Letters, 79, 1337-1340.

Mosey, N.J. and Carter, E.A. (2007) Ab initio evaluation of Coulomb and exchange parameters for DFT+U calculations. Physical Review B, 76, 1551231-15512313.

Monkhurst, H.J. and Pack, J.D. (1976) Special points for Brillouin-zone integrations. Physical Review B, 13, 5188-5192.

Nespolo, M. (2001) Perturbative theory of mica polytypism. Role of the M2 layer in the formation of inhomogeneous polytypes. Clays and Clay Minerals, 49.

Nieto, F. (2002) Characterization of coexisting NH_4- and K-micas in very low-grade metapelites. American Mineralogist, 87, 205-216.

Nieto, F., Mellini, M., and Abad, I. (2010) The Role of H_3O^+ in the Crystal Structure of Illite. Clays and Clay Minerals, 58, 238-246.

Payne, M.C., Teter, M.P., Allan, D.C., Arias, T.A. and Joannopoulous, J.D. (1992) Iterative minimization for ab initio total-energy calculations: molecular dynamics and conjugate gradients. Reviews of Modern Physics, 64, 1045-1097.

Perdew, J.P., Burke, K., and Ernzerhof, M. (1996) Generalized gradient approximation made simple. Physical Review Letters, 77, 3865-3868.

Pevear, D. R. (1999) Ilite and hydrocarbon exploration Proc. Natl. Acad. Sci., 96, 3440-3446.

Pfrommer, B.G., Côté, M., Louie, S., and Cohen, M.L. (1997) Relaxation of crystals with the Quasi-Newton Method. Journal of Computational Physics, 131, 233-240.

Refson, K., Tulip, P.R., and Clark, S.J. (2006) Variational density-functional perturbation theory for dielectrics and lattice dynamics. Physical Review B, 73. 1551141-15511412

Russell, J.D. and Fraser, A.R. (1970) I.R. spectroscopic evidence for interaction between hydronium ions and lattice OH groups in montmorillonite. Clays and Clay Minerals, 19, 55-59.

Shimanouchi, T. (1972) Tables of molecular vibrational frequencies consolidate Volume 1. National Bureau of Standards, 1-160.

Środoń J. (2009) Quantification of illite and smectite and their layer charges in sandstones and shales from shallow burial depth. Clay Minerals, 44, 421-434.

Stevenson, F.J. (1960) Nitrogeneous constituents of some palaezoic shales. American Association of Petroleum Geologists Bulletin, 44, 1257.

Sucha, V., Kraus, I., and Madejova, J. (1994) Ammonium illite from the anchimetamorphic shales associated with anthracite in the Zemplinicum of the Western Carpathians. Clay Minerals, 29, 369-377.

Vanderbilt, D. (1990) Soft self-consistent pseudopotentials in a generalized eigenvalue formalism. Physical Review B, 41, 7892-7895.

Wilcox, J. (2012) Carbon Capture. Springer, New York.

Williams, L.B. and Ferrell, R.E. (1991) Ammonium substitution in illite during maturation of organic-matter. Clays and Clay Minerals, 39, 400-408.

Williams, L.B., Wilcoxon, B.R., Ferrell, R.E., and Sassen, R. (1992) Diagenesis of ammonium during hydrocarbon maturation and migration, Wilcox Group, Louisiana, U.S.A. Applied Geochemistry, 7, 123-134.

Wilson, P.N., Parry, W.T., and Nash, W.P. (1992) Characterization of hydrothermal tobelitic veins from black shale, Oquirrh Mountains, Utah. Clays and Clay Minerals, 40, 405-420.

Yeh, L.I., Okumura, M., Myers, J.D., Price, J.M., and Lee, Y.T. (1989) Vibrational spectroscopy of the hydrated hydronium cluster ions H3O+(H2O)n (n=1,2,3). Journal of Chemical Physics, 91, 7319-7330.

Zhou, F., Cococcioni, M., Marianetti, C.A., Morgan, D., and Ceder, G. (2004) First-principles prediction of redox potentials in transition-metal compounds with LDA+U. Physical Review B, 70.

Zöller, M., and Brockamp, O. (1997) 1M- and $2M_1$-illite: different minerals and not polytypes. Eur. J. Mineral. 9, 821-827.

			T-sheet			O-sheet	
Model	I-M	K	Si	Al	Fe	Al	Mg
General formula -2M_1	-	1.67	6.68	1.32	0.38	3.29	0.32
NH_4^+	0.67	0.67	7.00	1.00	0.33	3.33	0.33
(Drits et al. 1997)	0.84	0.84	6.68	1.32	0.38	3.29	0.32
H_3O^+	0.33	1.00	7.00	1.00	0.33	3.33	0.33
(Nieto et al. 2010)	0.56	1.38	6.80	1.20	0.50	2.94	0.56
2I-H_2O	0.67	1.33	7.00	1.00	0.33	3.33	0.33
I-H_2O	0.33	1.00	7.33	0.67	0.33	3.33	0.33
(Nieto et al. 2010)	0.84	1.40	6.88	1.12	0.50	3.06	0.56

TABLE 1. Number of atoms for all types of models in this study, calculated per $O_{20}(OH)_4$. I-M is interlayer molecule other than K and varies for the ('particles from bulk') pfb-2M_1 models. The formula cited for Drits et al. (1997) is interpreted from the data within that reference, and the general formula for 2M_1 models.

Model/Ref	*a*	*b*	*c*	α	β	γ	Layer depths	
NH_4^+	5.23	9.08	20.67(29.89)	91.13	98.05	89.91	(NH_4^+)10.54	(K^+)10.13
(Drits et al. 1997)			20.31				(NH_4^+)10.33	(K^+) 9.98
H_3O^+	5.22	9.07	20.21(29.56)	90.36	95.47	89.83	(H_3O^+)10.20	(K^+)10.01
(Nieto et al. 2010)	5.22	9.04	20.04	90.00	95.90	90.00		
2I-H_2O	5.22	9.20	20.90(30.00)	90.00	95.67	90.00	10.45	10.45
(Nieto et al. 2010)	5.22	9.04	20.03	90.00	95.81	90.00		
I-H_2O	5.22	9.04	20.05(29.87)	90.37	96.25	89.88	(H_2O)10.18	9.87
(Nieto et al. 2010)	5.22	9.04	20.04	90.00	95.90	90.00		

TABLE 2. Lattice parameters of pfb-2M_1, sandwich cells of relaxed illite models in $\mathring{A}$ and degrees (relaxed *c*-length in brackets). The numbers without brackets of this study's models are the distances between the tetrahedral sheets of the bottom clay layer and the bottom of the uppermost clay layer, encompassing 2M_1 structures that are comparable to those cited. Drits et al. (1997) contains only the *c*-length estimate based on XRD data and the layer depths; Nieto et al. (2010) reports lattice parameters based on fixed and variable atomic coordinates of selected Rietveld refinements results of XRPD data. It should be noted that Nieto's H_3O^+ data are from a refinement of a Silver Hill illite, which is a 1M_d structure, with a high degree of rotational disorder, it is therefore difficult to ascribe the data solely to the presence of H_3O^+.

	NH_4^+				H_3O^+				I-H_2O				2I-H_2O			
Ring	4Si-2Al		5Si-Al/Si		4Si-2Al		5Si-Al/Si		4Si-2Al		5Si-Al/Si		4Si-2Al		5Si-Al/Si	
Angle	Si	Si-Al	Si	Si-Al	Si	Si-Al	Si	Si-Al	Si	Si-Al	Si	Si-Al	Si	Si-Al	Si	Si-Al
b-l min	112	110	111	110	110	108	109	108	108	99	103	101	120	112	116	117
b-l max	129	129	129	129	130	130	130	131	131	137	134	138	122	122	124	127
b-u min	-	-	110	-	-	-	109	-	-	-	108	-	-	-	114	-
b-u max	-	-	129	-	-	-	131	-	-	-	132	-	-	-	126	-
t-l min	99	85	90	85	96	86	90	87	101	91	94	91	92	87	89	88
t-l max	141	151	148	152	144	149	148	151	139	145	144	147	144	149	149	151
t-u min	-	-	116	-	-	-	107	-	-	-	116	-	-	-	113	-
t-u max	-	-	124	-	-	-	133	-	-	-	123	-	-	-	127	-

TABLE 3. Minimum (‘min’) and maximum (‘max’) Si-Si-Si (‘Si’) and Si-Al-Si and permutations, (‘Si-Al’) internal angles of the hexagonal Si-O cavities (‘Ring’) comprising 4 Si plus 2 Al (‘4Si-2Al’); 5 Si plus 1 Al (‘5Si-Al’) or 6 Si (‘5Si-Si’), as seen from the bottom (‘b’) and top (‘t’) interlayer spaces, projected onto the lower (‘l’) and upper (‘u’) clay mineral layers. Figure 2 illustrates these cavities and interlayer molecules. Angles are in degrees to the nearest integer.

Model	Scissor	Wag	Rock	Sym-stretch	Antisym-stretch
NH_4^+	1392	1454	1652	3172	3338
	1369	1504	1657	3223	3369
	1406	1627	1666	3274	3436
	1427			3286	3552
				3552	
H_3O^+	1576				2747
	1668			2854	3110
					(single OH)
I-H_2O	1640			3651	3708

TABLE 4. Description of the vibrational frequencies (cm^{-1}) of three of the pfb-$2M_1$ models. 'Sym' and Antisym' mean 'symmetric' and 'antisymmetric' respectively.

	50% of layers with NH_4^+			A: d_{00c} spacing ($\mathring{A}$); B: 2θ (°)			
	FWWH(00a)	FWWH(00b)	$\frac{\text{FWWH}(00b)}{\text{FWWH}(00a)}$	NH_4^+	H_3O^+	I-H_2O	2I-H_2O
This study	0.1033	0.1501	1.45	A: 9.86	9.81	9.90	9.95
(a:6, b:15, c:3)				B: 8.96	9.01	8.93	8.88
Drits et al. (1997)	0.885	1.266	1.43	A: 10.19	-	-	-
(a:2, b:5, c:1)							

TABLE 5. Left - full width at half height (FWHH) measurements in degrees, given for d_{hkl} and compared to the data of Drits et al. for 50% of layers containing NH_4^+. Right - rows A: d_{003} and d_{001} layer measurements; row B: 2θ angles corresponding to the d_{003} peaks in our study.

Figure 1. Single unit cells of ('particles from bulk') pfb-$2M_1$ after relaxation and their formulae per $O_{20}(OH)_4$. Vacuum space at top of models defines them as particle models. Initial cell parameters for all four varieties were: $a = 5.22$; $b = 9.02$; $c = 30.00$; $\alpha = 90.00$; $\beta = 95.67$; $\gamma = 90.00$. Color scheme used throughout this study: oxygen - red; hydrogen - white; aluminum - pink; silicon - yellow; iron - gray-blue; potassium - purple; magnesium - green; nitrogen - blue. The dashed line is the periodic boundary of a unit cell. All lengths throughout this work (to 2 decimal places) are in $\mathring{A}$ and angles in degrees.

Figure 2. Polygon-view of positions of interlayer molecules relative to clay mineral layers, where 'b' is bottom interlayer; 't' is top interlayer; 'l' is relative to lower clay layer; 'u' is relative to upper clay layer; 's' is side view, for example, 'b-u' shows the positions of the bottom interlayer molecules relative to the upper clay layer enclosing them. All non-side views are $x - y$ plane views.

Figure 3. Simulated X-ray powder diffraction (XRPD) patterns.

Figure 4. XRD patterns calculated from the relaxed molecular modeled structures compared with an XRD pattern calculated for a trans vacant $2M_1$ mica, with an iron free composition of $K_{0.8}(Al_{0.8}Si_{3.2})(Al_2)O_{10}(OH)_2$ - further details are in the XRPD Section.

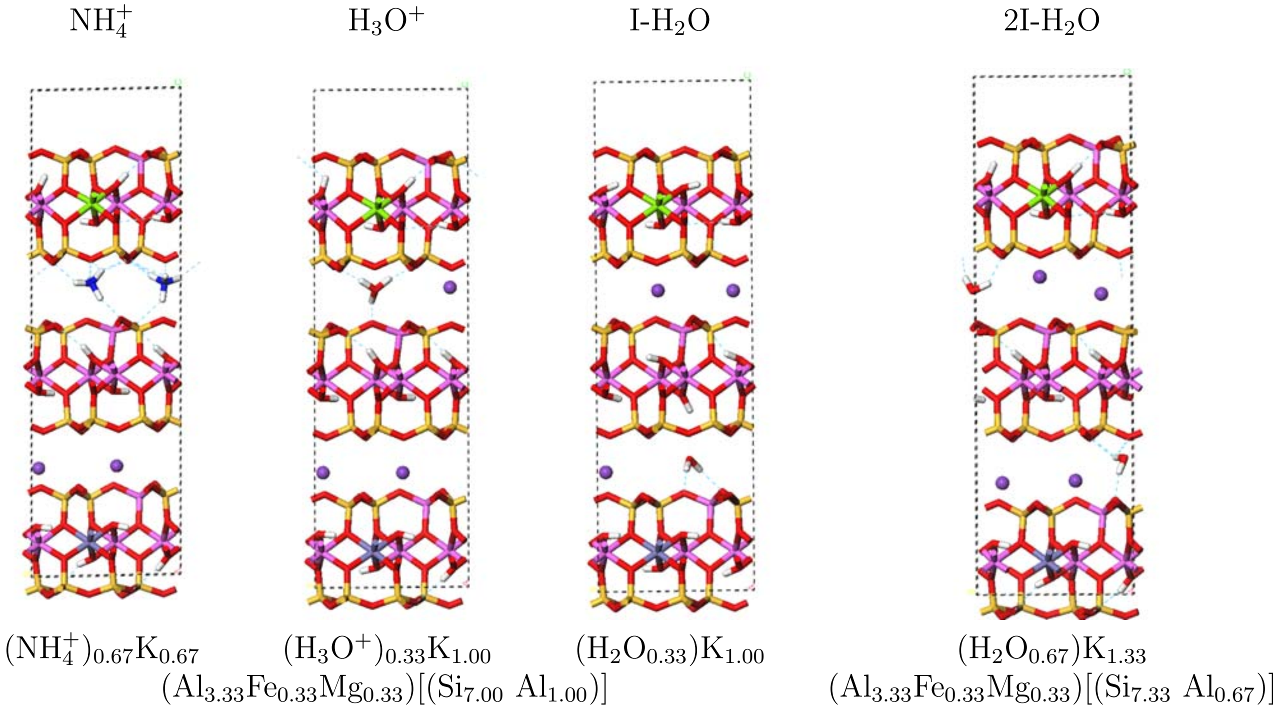

NH_4^+ H_3O^+ I-H_2O 2I-H_2O

$(NH_4^+)_{0.67}K_{0.67}$ $(H_3O^+)_{0.33}K_{1.00}$ $(H_2O_{0.33})K_{1.00}$
$(Al_{3.33}Fe_{0.33}Mg_{0.33})[(Si_{7.00}\ Al_{1.00})]$

$(H_2O_{0.67})K_{1.33}$
$(Al_{3.33}Fe_{0.33}Mg_{0.33})[(Si_{7.33}\ Al_{0.67})]$

FIGURE 1. Single unit cells of ('particles from bulk') pfb-2M_1 after relaxation and their formulae per $O_{20}(OH)_4$. Vacuum space at top of models defines them as particle models. Initial cell parameters for all four varieties were: $a = 5.22$; $b = 9.02$; $c = 30.00$; $\alpha = 90.00$; $\beta = 95.67$; $\gamma = 90.00$. Color scheme used throughout this study: oxygen - red; hydrogen - white; aluminum - pink; silicon - yellow; iron - gray-blue; potassium - purple; magnesium - green; nitrogen - blue. The dashed line is the periodic boundary of a unit cell. All lengths throughout this work (to 2 decimal places) are in $\mathring{A}$ and angles in degrees.

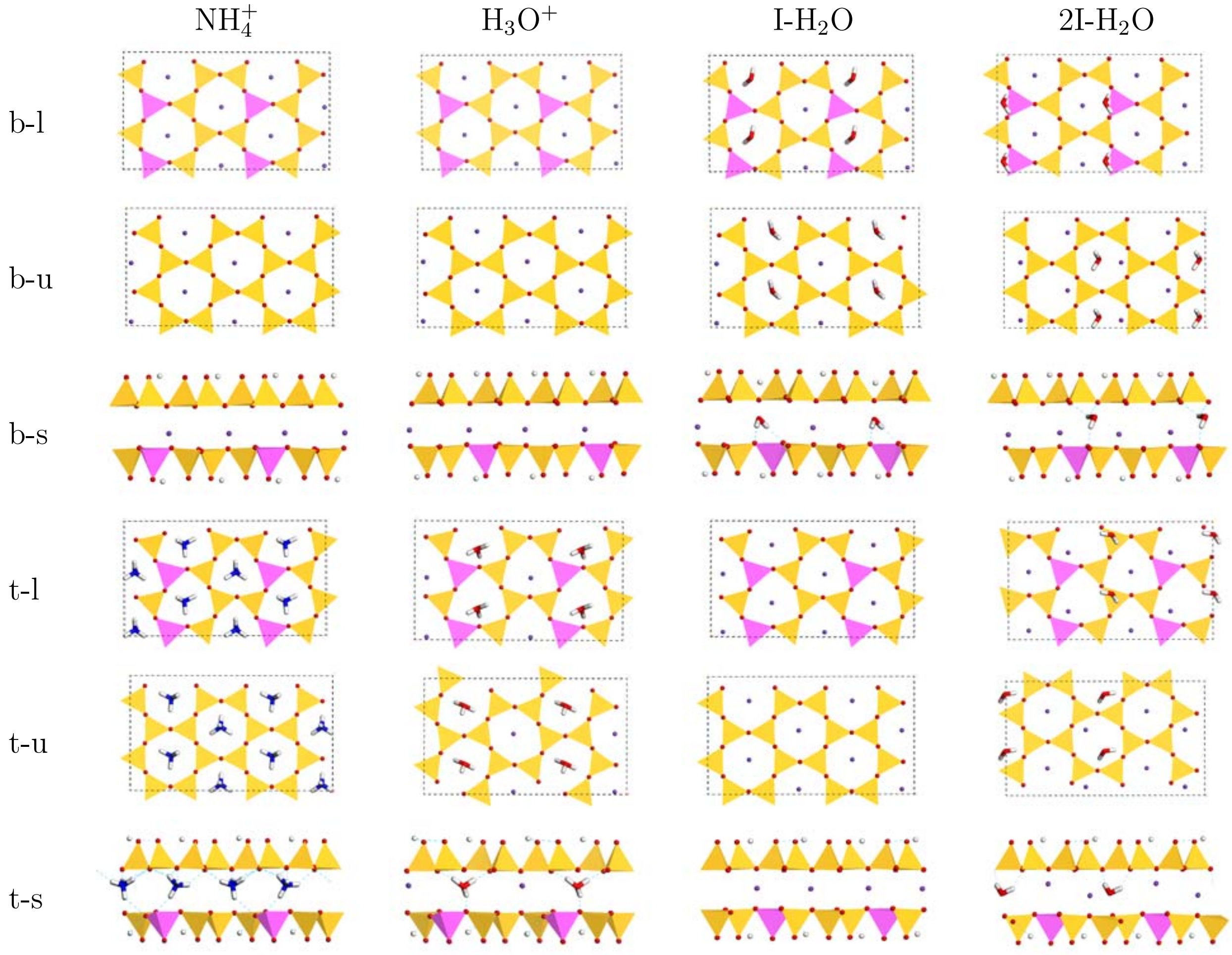

FIGURE 2. Polygon-view of positions of interlayer molecules relative to clay mineral layers, where ‘b’ is bottom interlayer; ‘t’ is top interlayer; ‘l’ is relative to lower clay layer; ‘u’ is relative to upper clay layer; ‘s’ is side view, for example, ‘b-u’ shows the positions of the bottom interlayer molecules relative to the upper clay layer enclosing them. All non-side views are $x - y$ plane views.

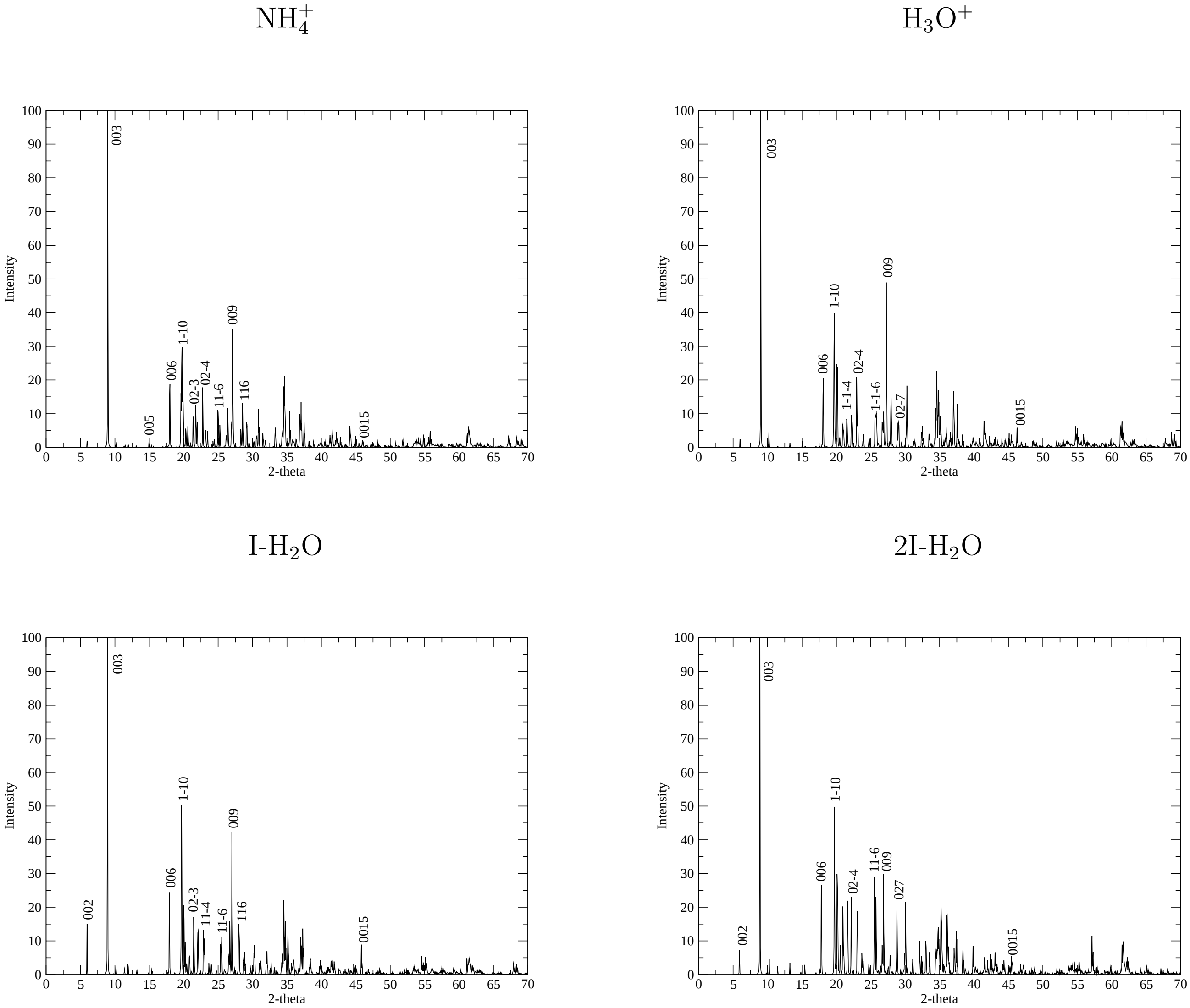
NH_4^+

H_3O^+

$I\text{-}H_2O$

$2I\text{-}H_2O$

FIGURE 3. Simulated X-ray powder diffraction (XRPD) patterns

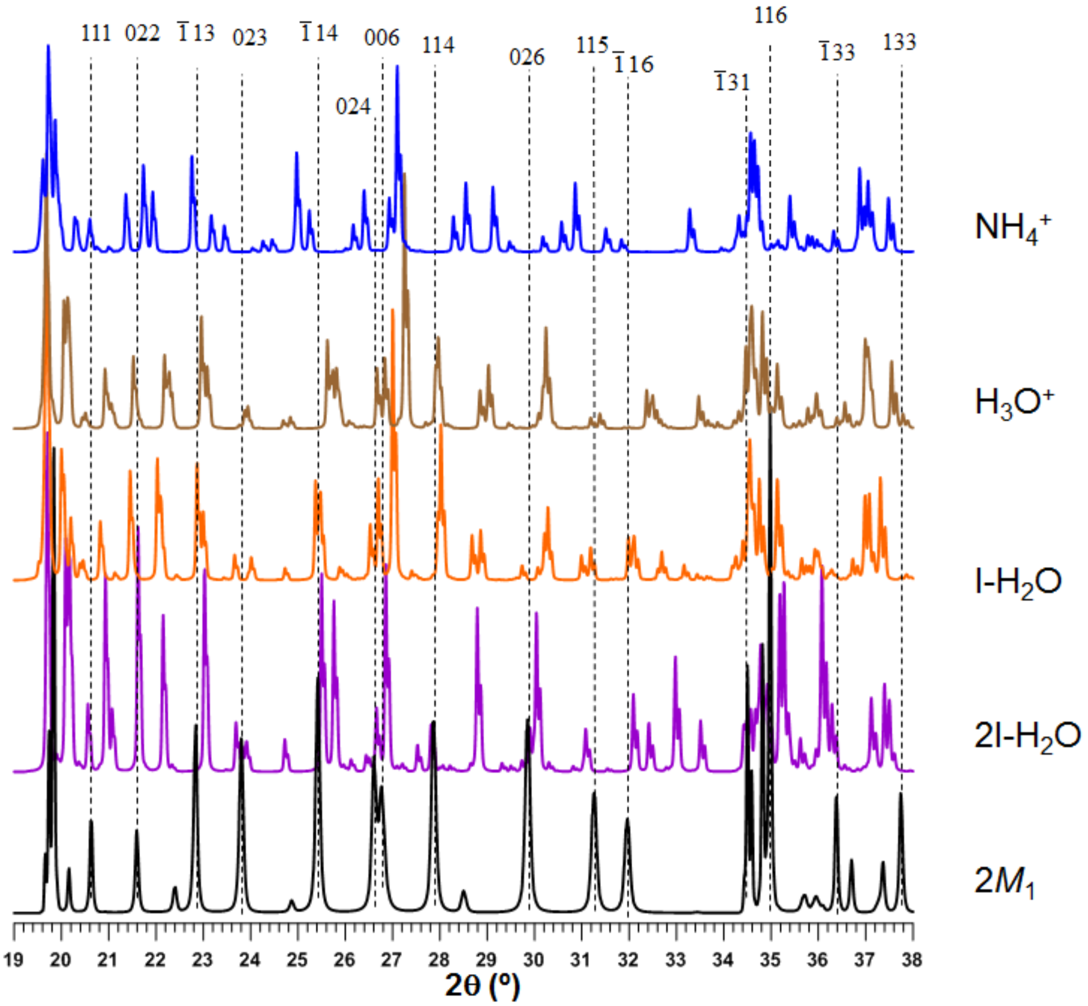

FIGURE 4. XRD patterns calculated from the relaxed molecular modeled structures compared with an XRD pattern calculated for a trans vacant $2M_1$ mica, with an iron free composition of $K_{0.8}(Al_{0.8}Si_{3.2})(Al_2)O_{10}(OH)_2$ - further details are in the XRPD Section.